Published in final edited form as:
J Phys Chem C Nanomater Interfaces. 2011 April 21; 115(19): 9432–9441. doi:10.1021/jp201213g.

Multi-technique Characterization of Self-assembled Carboxylic Acid Terminated Alkanethiol Monolayers on Nanoparticle and Flat Gold Surfaces

Sirnegeda D. Techane, **Lara J. Gamble**, and **David G. Castner***
National ESCA and Surface Analysis Center for Biomedical Problems, Departments of Chemical Engineering and Bioengineering, University of Washington Box 351750, Seattle, WA 98195-1750, USA

Abstract

Gold nanoparticles (AuNPs) with 14, 25 and 40nm diameters were functionalized with different chain length (C6, C8, C11 and C16) carboxylic acid terminated alkanethiol self-assembled monolayers (COOH-SAMs). X-ray photoelectron spectroscopy (XPS) and time-of-flight secondary ion mass spectrometry (ToF-SIMS) were used to examine the changes in surface chemistry as both AuNP diameter and SAM chain length were varied. COOH-SAMs on flat gold surfaces were also examined and compared to the COOH-SAM on AuNP results. For a given surface, as the COOH-SAM chain length increased the XPS C/Au atomic ratio increased due to an increased number of carbon atoms per molecule in the overlayer and an increased attenuation of the Au substrate signal. For the C16 COOH-SAMs, as the size of AuNPs decreased the XPS C/Au atomic ratio and the apparent SAM thickness increased due to the increased curvature of the smaller AuNPs. The C16 COOH-SAMs on the flat Au had the lowest XPS C/Au atomic ratio and apparent SAM thickness of any C16 COOH-SAM covered Au surface. The effective take-off angles of the COOH-SAMs were also calculated by comparing the apparent thickness of COOH-SAMs with literature values. The effective take-off angle for C16 COOH-SAM on 14nm, 25nm and 40nm diameter AuNPs and flat Au were found to be 57°, 53°, 51° and 39°, respectively, for data acquired in a mode that collects a wide range of photoelectron take-off angles. The effective take-off angle for C16 COOH-SAM on 14nm AuNP and flat Au decreased to 52° and 0°, respectively, for data acquired in a mode that collects a narrow range of photoelectron take-off angles. The ToF-SIMS results showed similar changes in surface chemistry with COOH-SAM chain length and AuNP size. For example, the ratio of the sum of the $C_{1–4}H_xO_y$ positive ion intensities to the sum of the Au-containing positive ions intensities increased with decreasing AuNP size and increasing COOH-SAM chain length. Fourier transform IR spectroscopy in the attenuated total reflectance mode (FTIR-ATR) was used to characterize the crystallinity of the COOH-SAMs. The CH_2 stretching frequencies decreased with increasing COOH-SAM chain length on flat Au. The C16 COOH-SAM on the 14nm AuNPs exhibited a crystalline-like CH_2 stretching frequency. The size, size distribution, shapes and solution stability of AuNPs were investigated with transmission electron microscopy (TEM) and UV/VIS spectroscopy. As the average diameter of the AuNPs decreased the size distribution became narrower and the shape became more spherical.

*Corresponding Author: Prof. David G. Castner, Department of Chemical Engineering, University of Washington, Box 351750, Seattle, WA 98195-1750, 1-206-543-8094, castner@nb.uw.edu.

6. Supporting Information

ImageJ analysis of 25nm and 40nm size and circularity distribution, PCA scores and loadings results, discussion about the UV/VIS spectroscopy results for the 14, 25 and 40nm AuNPs functionalized with C6, C8, C11 and C16 COOH-SAMs, and the FTIR-ATR spectrum for C16 COOH-SAM on 14nm AuNPs are provided in the supporting information.

1. Introduction

Gold nanoparticles (AuNPs) in the size range of 1–100nm with shapes varying from spherical to polygons are being used in a wide range of applications. [1–12] AuNPs have a high percentage of surface atoms and, therefore, significantly different reactivities compared to bulk gold samples. [1,13] Consequently, size and surface chemistry play critical roles in determining the overall properties of nanoparticles. For example, they give AuNPs their specific characteristic surface plasmon and surface reactivity. [13] Despite the widespread appreciation of the unique properties of high surface area nanoparticles there is a surprising lack of detailed surface characterization of these materials, especially for nanoparticles used in biomedical applications.[14] The surface characterization of nanoparticles does present significant challenges, [15] so it is essential to investigate model systems with well-defined, systematic variations of surface properties in order to develop the needed comprehensive surface characterization methodology.

Theoretical and experimental studies of monolayer protected gold nanocrystals (MPCs) with diameters < 5nm by Luedtke et al. [8,16] and Hostetler et al. [7] have demonstrated the significance of nanoparticle size on the self-assembled monolayer (SAM) properties. The AuNP size and surface functionalization chemistry can be controlled to take advantage of the unique nanoparticle properties. Important aspects of AuNP surface functionalization include the thickness of the added overlayer and location of functional groups within that overlayer. It is well established that x-ray photoelectron spectroscopy (XPS) can provide overlayer thickness and functional group location for thin films on flat surfaces. [9] This is typically done through a combination of angle-resolved XPS measurements and a Beer's law analysis of the overlayer and substrate intensities. [9] The challenge is extending this capability to AuNPs, since now the measured overlayer and substrate intensities also depend on particle size. [5,17,18] Thus, studies are needed where both the AuNP size and the overlayer thickness are systematically varied to assess the contribution of surface curvature on the XPS overlayer and substrate intensities.

A desired range of AuNPs sizes can be obtained through previously published synthesis methods. [2,10] For example, AuNPs with diameters >12nm can be prepared by reduction of $HAuCl_4$ with sodium citrate, a method developed by Turkevich et al. [11] and later refined by Frens [4]. There are some advantages of larger AuNPs over the smaller MPC. For example, in studies that utilize chemiluminescence, it is preferred to use larger AuNPs. [3,12] Also, the SAMs formed on larger AuNPs are expected to be more comparable to SAMs formed on flat Au surfaces. [16] Thus, AuNPs with diameters in the 10 to 100nm range are a good starting point for addressing how surface curvature affects the measured XPS overlayer (SAM) and substrate (Au) intensities since SAMs on flat Au surfaces can be used as references.

Optimizing the performance of AuNPs for a desired application relies on the success of designing and achieving the right AuNP surface functionalization. Since the first studies of functionalizing AuNPs with thiols [6], various ligands and functionalization techniques have been explored. [19–25] Most design strategies that involve simultaneous AuNP formation and surface functionalization produce MPCs. [26–31] For larger AuNPs (which will be simply referred hereafter as AuNPs), functionalization is typically done after their synthesis is complete. Functionalization of AuNPs with ligands that have hydrophobic and positively charged terminal-groups may require extra functionalization steps to avoid AuNP aggregation. [32] Functionalization of AuNPs with ligands that have negatively charged end-groups, such as carboxylic acid terminated thiols, have been shown to present fewer AuNP aggregation challenges. [23,32] Also, carboxylic acid thiols have been shown to form well ordered SAMs on flat Au surfaces. [33]

A multiple technique approach that includes XPS and time-of-flight secondary ion mass spectrometry (ToF-SIMS) has been a powerful method for obtaining detailed surface characterization of SAMs on flat Au surfaces.[34–39] Unfortunately to date, detailed XPS and ToF-SIMS investigations of AuNP surface chemistry are the exception. Typical methods used to characterize AuNPs include transmission electron microscopy (TEM), Fourier transform IR (FTIR) spectroscopy and UV/VIS spectroscopy. These techniques provide valuable information about AuNPs, but it is challenging to extract detailed, quantitative information about overlayer thickness, location of specific functional groups in the overlayer, presence of contaminants, extent of functionalization, etc. using just these techniques. Thus, there is a need to incorporate the surface sensitivity and chemical specificity of XPS and ToF-SIMS into multi-technique characterization studies of AuNPs.

The objective of this study is to prepare a set of well-defined SAM functionalized AuNPs that can be used to investigate the effect of AuNP size and surface organic layer thickness with XPS and ToF-SIMS. Carboxylic acid terminated alkanethiol SAMs on AuNPs (COOH-SAM/AuNPs) and flat Au surfaces (COOH-SAM/Au) were selected for this purpose. Both the AuNPs size (14, 25 and 40nm diameters) and carboxylic acid alkanethiol chain length (C6, C8, C11 and C16) were varied. The crystallinity of the COOH-SAM functionalized surfaces were examined by attenuated total reflectance FTIR (FTIR-ATR). The size, size distribution and shape of the AuNPs were characterized with TEM and their solution stability was characterized by UV/VIS spectroscopy. This study provides a detailed, complementary approach for surface characterization of well-defined, functionalized AuNPs as well an assessment of curvature effects (i.e., AuNP size) on the XPS and ToF-SIMS measurements.

2. Experimental Section

2.1. Materials

The following chemicals were purchased from Sigma-Aldrich and used as received: gold (III) chloride hydrate ($HAuCl_4 \cdot xH_2O$, x = ~3; 99.999%), trisodium citrate dihydrate ($C_6H_5Na_3O_7.2H_2O$, 99.5%), 6-mercaptohexanoic acid ($HS(CH_2)_5CO_2H$, 90%), 8-mercaptooctanoic acid ($HS(CH_2)_7CO_2H$, 96%), 11-mercaptoundecanoic acid ($HS(CH_2)_{10}CO_2H$, 95%), 1-octanethiol ($HS(CH_2)_7CH_3$, 98%), 1-undecanethiol ($HS(CH_2)_{10}CH_3$, 98%) and 1-hexadecanethiol ($HS(CH_2)_{15}CH_3$, 99%). 16-mercaptohexadecanoic acid ($HS(CH_2)_{15}CO_2H$, 90%) was purchased from Asemblon and used as received. Additional reagents (company, concentration, grade) included HCl (EMD Chemicals Inc., 36.5–38%, ACS), HNO_3 (EMD Chemicals Inc., 68.0–70.0%, ACS), NH_4OH (J.T. Baker Inc., 28.0–30.0% as NH_3, ACS), and ethanol (AAPER, absolute-200 proof). Ultrapure water (resistivity >18.0 M Ω cm) was purified by a Modulab Analytical research grade water system.

Dialysis tubing (Spectra/Por, regenerated cellulose, MWCO of 12,000 – 14,000 and 50,000) was purchased from VWR Scientific Inc. Corning Plastic Filter System (50 mm membrane) was purchased from Fisher Scientific. TEM grids (Carbon Type-A, 300 mesh, copper grids) were purchased from Ted Pella. Silicon wafers were purchased from Silicon Valley Microelectronics, and diced to 0.6–1cm × 1cm then thoroughly cleaned with a series of organic solvents. Flat gold substrates were prepared by coating the cleaned silicon wafers with 10nm titanium followed by 100nm gold (99.99%) using a CHA 600 Electron Beam Evaporator at pressures below 1×10^{-6} Torr. Typical rms roughness of the as deposited gold films, as determined by atomic force microscopy measurements, was 1.6±0.4 nm over a 2.0 μm × 2.0 μm area.

2.2. Preparation of AuNPs

Three different sizes of AuNP (14, 25 and 40nm) were synthesized by citrate reduction methods as reported by Frens [4]. Briefly, all glassware were cleaned with aqua regia (HCl: HNO_3 in the ratio of 3:1) and rinsed with ultrapure water prior to use. First, a 0.01% (w/v) $HAuCl_4$ aqueous solution was heated to 100°C under a reflux system. Then, a 1% (w/v) trisodium citrate aqueous solution was added to the refluxing solution. Volumetric ratios of 2.5:100, 1.5:100 and 1:100 for the trisodium citrate and $HAuCl_4$ aqueous solutions were used to make 14, 25 and 40nm average diameter AuNPs, respectively. The reaction was allowed to continue for 30 minutes. The final AuNP solutions were cooled to room temperature before analysis and functionalization.

2.3. Functionalization of AuNPs with COOH-SAMs

NH_4OH was added to the AuNP solutions before adding thiol (for 40nm AuNPs) and after adding thiol (for 14 and 25nm AuNPs) to adjust their pH to >11. An excess amount (2x) of 1mM carboxylic thiol in ethanol was added to the AuNP solutions. The solutions were then sonicated for ~5 minutes to break apart any thiol induced aggregation, and stirred for ~24hrs to allow formation of the COOH-SAMs. The AuNP COOH-SAM solutions were filtered to remove large impurities. Then the samples were first dialyzed 3x with 14K MWCO tubing, which is compatible with the basic solution. Final dialysis used the 50K MWCO tubing with multiple water changes to further remove excess thiol and ions. We observed that purifying the COOH-SAM/AuNPs by dialysis instead of the more common centrifugation/re-dispersal methods was an easier method for generating high-quality functionalized AuNPs. Using the centrifugation/re-dispersal method it was common to detect the presence of overlayers that were greater than a monolayer in thickness along with unbound and oxidized sulfur species (data not shown), indicating that dialysis is a more effective method for removing physisorbed thiol molecules.

2.4. Preparation of AuNP samples for characterization measurements

About 1mL of the purified solutions was retained for UV/VIS measurements and the rest was 4–5x concentrated by centrifugation at 13K RPM for average of 1hr. For surface chemistry characterization with XPS and ToF-SIMS, ~100μL of each concentrated solution was placed onto a clean silicon substrate and allowed to dry in a desiccator. This step was repeated until a complete layer of AuNPs was formed on the substrate to minimize the substrate Si signal during XPS and ToF-SIMS measurements. These samples were stored in a petri-dish backfilled with N_2 gas until the surface analysis measurements were made. For FTIR-ATR analysis, the concentrated solution was dried so that it completely covered a 1cm × 1cm Si substrate with a thicker layer of AuNPs. For size and shape characterization with TEM, ~7μL of each sample solution was placed on a TEM grid and allowed to air-dry on filter paper prior to analysis.

2.5. Functionalization of flat Au with COOH and CH_3 SAMs

Clean Au substrates were immersed in 5mL of a 1mM thiol solution in ethanol and backfilled with N_2 gas. After ~24hrs incubation at room temperature the substrates were removed and rinsed by squirting excess ethanol over them to remove unbound thiols. For the COOH SAM, additional rinsing was performed by placing the substrate in fresh ethanol and sonication for 5min to remove H-bonded thiols. Immediately after sonication, the substrates were again rinsed extensively with ethanol and blown dry with N_2 gas. All samples were stored in petri-dishes backfilled with N_2 gas until surface analysis measurements were done.

2.6. Transmission Electron Microscopy (TEM)

TEM measurements were performed on Philips CM100 instrument operating at 100kV accelerating voltage. It was equipped with a Galan Model 689 digital slow scan camera. Pictures with 128×128 pixels were taken for each AuNPs sample typically in the range of 130K–180K magnification. ImageJ software was used to analyze the average diameter, size distribution and circularity of AuNPs from the TEM pictures, which were based on data from approximately 500–1000 particles for each type of AuNPs.

2.7. X-ray photoelectron spectroscopy (XPS)

Except where specified, XPS measurements were performed on a Kratos AXIS Ultra DLD (Kratos, Manchester, UK) instrument in the 'hybrid' mode using a monochromatic A1 Kα X-ray source and a photoelectron take-off angle of 0° (the take-off angle is defined as the angle between the substrate normal and the axis of the analyzer lens). The hybrid mode is commonly used by XPS analysts as it provides a strong signal due to the wide range of photoelectron take-off angles accepted by the analyzer in this mode. For each sample a survey scan from 0 – 1100eV binding energy (BE) and elemental scans of S 2p and (Si 2p for AuNPs) were measured using a pass energy of 80eV on three spots to identify the species present and determine XPS elemental compositions. High-resolution scans of the C 1s, S 2p, and Au 4f peaks were acquired from one spot on each sample using a pass energy of 20eV to examine the type of chemical species present. All AuNP samples were run as insulators using a low-energy flood gun for charge neutralization. Measurements were repeated on two or more replicates for each sample. Additional Kratos XPS data were taken at the 0° take-off angle in the electrostatic mode for selected samples. In the electrostatic mode only a narrow range of photoelectron take-off angles are accepted by the analyzer. This results in a significantly weaker signal compared to the hybrid mode. Data analysis was performed with Vision Processing data reduction software. All BEs were referenced to the C 1s hydrocarbon peak at 285 eV.

2.8. Time of flight secondary ion mass spectrometry (ToF-SIMS)

ToF-SIMS measurements were performed on an ION-TOF TOF.SIMS 5 instrument (ION-TOF, Münster, Germany) using a Bi^+ primary ion source. The primary ion beam had 45° angle of incidence with respect to the substrate surface. For each sample, three positive and three negative ion static SIMS spectra were acquired on six different 100μm × 100μm areas. Mass resolutions (m/Δm) at the $C_2H_3^+$ (m/z = 27) and C_2H^- (m/z = 25) peaks were typically above 6000 in both the positive and negative ion spectra. The positive spectra were mass calibrated to the CH^+, CH_2^+, $C_2H_2^+$ peaks. Principal component analysis (PCA) of the negative spectra did not show any identifiable trends and therefore are not included here. PCA was performed on the ToF-SIMS data as described previously by Wagner et al. [40]. Peaks having an intensity of >50 counts were included in the initial PCA peak list. Then after the initial PCA processing, peaks with the 200 largest absolute magnitude loadings were selected for further analysis after removing peaks from contamination and pure gold. All spectra were mean-centered and normalized by the sum of the intensities of the selected peaks prior to PCA.

2.9. UV/VIS spectroscopy

UV/VIS absorption measurements were performed on a Hewlett Packard 8452A Diode Array spectrophotometer. Absorbance measurements were taken over the 200 – 1100nm wavelength range for each of the AuNP samples. Relative shifting and broadening of the main absorbance peak, which is centered between 515 – 550nm, and additional peaks at higher wavelength were used to characterize and compare stability of the AuNPs samples.

2.10. FTIR-ATR

FTIR-ATR measurements were performed on a Bruker Tensor spectrometer with a germanium ATR crystal in the mid-IR frequency range (4000 – 400cm^{-1}). A spectrum was acquired with a minimum of 100 scans at 4cm^{-1} resolution. The crystallinity of the SAM on the surfaces was determined by the position of the CH stretching vibrations peaks ($\upsilon CH_{2,\ asym}$ and $\upsilon CH_{2,\ sym}$). The fingerprint region (950 – 1500cm^{-1}) was also examined for the presence of known and expected peaks.

3. Results and Discussions

3.1. TEM Analysis

TEM images for the three different sizes of AuNP samples and the ImageJ analysis for 14nm AuNPs are shown in Figure 1 (see Supporting Information for the other sizes). The 14nm AuNPs had a narrow size distribution (standard deviation of 0.9nm) and ~86% of the AuNPs had a major-axis/minor-axis ratio <1.1. The 14m AuNPs were more spherical compared to the 25nm and 40nm AuNPs that had ~56% and ~38% of the AuNPs, respectively, with a major-axis/minor-axis ratio <1.1.

3.2. XPS Analysis

XPS elemental compositional measurements of the AuNP samples showed the presence of all surface atoms expected from the overlayer COOH-SAMs (C, O and S) and core NPs (Au). XPS determined elemental compositions for the C16, C11, C8 and C6 chain length COOH-SAMs on the 14nm AuNP and flat Au samples are shown in Table 1. XPS determined elemental compositions for the C16 COOH-SAM on the 14nm, 25nm, and 40nm AuNPs and flat Au samples are shown in Table 2. Small amounts Si from the underlying Si wafer substrate was also detected on the following samples (Si atomic %): 14nm AuNPs with the C16 COOH-SAM (1.6%), with the C11 COOH-SAM (1.6%), with the C8 COOH-SAM (0.2%) and with the C6 COOH-SAM (0.0%); 40nm AuNPs with the C16 COOH-SAM (0.7%); and 25nm AuNPs with the C16 COOH-SAM (0.9%). To remove the contributions from the Si substrate, the proportional values from the measured composition of a bare Si surface (Si = 59.8 atomic %, O = 28.3 atomic % and C = 11.9 atomic %) were subtracted from the AuNP samples and the data was then renormalized. Some of the COOH-SAM on flat Au had Zn contamination. The average Zn atomic % was 1.1, 0.4, 0.4 and 0.3 for C16, C11, C8 and C6 COOH-SAMs, respectively. COOH-SAM on flat Au samples prepared in the presence of HCl did not have the Zn contamination; however these samples had lower C% indicating lower SAM coverage (data not shown). These results suggest that the Zn was attracted to the negative charge present on the COOH-SAMs prepared without HCl. The average atomic percent compositions shown in Table 1 and 2 have been renormalized to exclude Si and Zn for AuNP and flat Au samples, respectively. Since the atomic % Si and Zn were small (1 atomic % or lower in most samples), the corrections were small and should not have a significant effect on the results and conclusions of this study.

The XPS C/Au atomic ratio is commonly used to analyze surface compositional changes between different SAMs on surfaces. [41] Figure 2 shows the trend in the C/Au atomic ratio as the SAM chain lengths and surface types were varied. The ratio increased going from the shorter chain (C6) to the longer chain (C16) COOH-SAM (Figure 2a), as expected due to the increased number of carbon atoms in the longer chain molecules. Also, the longer chains form thicker SAMs, which lead to increased attenuation of the Au signal from the core of the NPs.

The XPS C/Au atomic ratio for the C16 COOH –SAMs decreased as the AuNP size increased and was the smallest on the flat Au surface (Figure 2b). (The C11, C8 and C6

COOH-SAMs exhibited similar trends - data not shown). This change in XPS C/Au atomic ratio can be attributed to the decrease in surface curvature from the smallest AuNPs to the flat Au samples. [15] For flat surfaces, XPS data are typically comprised of signals from a narrow range of photoelectron take-off angles. For NPs, XPS data contains signals from all photoelectron take-off angles. [5] Since the ratio of overlayer (i.e., SAM) signals to underlayer (i.e., AuNP) signals for a given overlayer thickness varies with photoelectron take-off, it is expected the C/Au atomic ratio should vary with AuNP size for the C16-COOH SAM/AuNP system. For a C16-COOH SAM on a flat Au surface the C/Au atomic ratio will be the smallest at a 0° photoelectron take-off angle since that experiment condition results in the largest XPS sampling depth (i.e., strongest Au signal). As the photoelectron take-off angle is increased the measured C/Au atomic ratio will increase due to the decrease in the XPS sampling depth. [9] Since the XPS COOH-SAM/AuNP system data is a weighted average from all photoelectron take-off angles, the C/Au atomic ratios will be higher than observed from flat Au surfaces and will depend on AuNP size.

In results reported elsewhere, XPS surface compositions from simulation and measurement for the C16 COOH-SAM on a flat surface at photoelectron take-off angles over a range of 45 to 55° had similar XPS surface compositions to the C16 COOH-SAM on the 14nm AuNPs. [42] The results from these studies indicate that using measurements of photoelectrons over a range of take-off angles from 5 to 85° in conjunction to SESSA (Simulation of Electron Spectra for Surface Analysis)[43–45] for C16 COOH-SAM on flat Au can provide good estimates of the overlayer thickness of the SAM on spherical AuNPs. Gunter et al. [46] found that topography effects can be minimized for calculating overlayer thickness on rough surfaces by using take-off angles over a range of angles from 40 – 45°. These ‘magic angles’, were shown to introduce an average error of less than 10%. Other similar studies found the ‘magic angle’ to be approximately 50–55° after taking into account neighbor-shadowing effects for rough surface topographies. [17,47] Shard et al. [17] used Topofactor to estimate the overlayer thickness for spherical macroscopic samples – where overlayer thickness for a flat surface was first calculated using the Thickogram method [48] then multiplied by a 0.67 Topofactor. They reported that the Topofactor method was not applicable to nanoparticle systems. Frydman et al. [5] used more detailed mathematical formulas to evaluate XPS intensities from powdered catalyst particles and determine the surface structural model for supported particles. They reported that using unweighted average take-off angle of 57.3° for their formula could result in as much as 23% error. [5]

Here we performed a simple calculation to approximate the overlayer thickness and effective take-off angle for the COOH-SAM on flat Au and AuNP surfaces based on Equation 1.[49]

$$d=\lambda_{avg}\, Cos\theta\, \mathrm{Ln}[\,1+\frac{I_c}{I_{Au}}\cdot\frac{I^o_{Au}}{I^o_c}\,] \qquad (1)$$

where d is the overlayer thickness for COOH-SAM; λ_{avg} is the average inelastic mean free path based on λ_c (~30Å) and λ_{Au} (~33Å) for photoelectrons passing through the SAM overlayer; θ is the take-off angle from the surface normal; I_c and I_{Au} are the measured intensities for C1s and Au4f in terms of their areas, respectively; and I^o_C and I^o_{Au} are the intensities for pure elements C and Au and their ratio is calculated using Equation 2. [49]

$$\frac{I^{o}_{Au}}{I^{o}_{c}} = \frac{N^{o}_{Au}\lambda_{Au}(E_{Au})G(E_{Au})}{N^{o}_{c}\lambda_{c}(E_{c})G(E_{c})} \quad (2)$$

where N^{o}_{Au} and N^{o}_{C} are the number density and their ratio was calculated based on 19.3g/cm^3 and 1.2g/cm^3 for Au and the SAM, respectively, and $G(E_{Au})$ and $G(E_c)$ are the spectrometer transmission as a function of the photoelectron kinetic energy, which was equal to 3.2 and 4.0, respectively, for the Kratos XPS instrument operated in the hybrid mode.

The apparent COOH-SAMs thickness calculated from the above equations using measured intensities at 0° take-off angle in hybrid mode (d_H) and measured intensities at 0° take-off angle in electrostatic mode (d_E) are shown in Table 3. The thickness from ellipsometry measurements for COOH-SAMs on flat Au from literature (d_L) are also shown in Table 3. We used the equation $d_L = 1.16n + 4.8$ for COOH $(CH_2)_n$ SH where n is equal to 5, 7, 10 and 15 to calculate d_L for C6, C8, C11 and C16 COOH-SAM, respectively. [50] In all cases, d_H was larger than the corresponding d_L. The difference in the apparent SAM thickness from the two XPS analysis modes is a result of the wider analyzer acceptance angle in the hybrid mode compared to the electrostatic mode. For all COOH-SAMs on flat Au measured at 0° in the electrostatic mode, the d_E was within experimental error of the corresponding d_L. On the other hand, for C16 COOH-SAM on 14nm AuNP, the d_E was about 60% greater than its d_L due the full range of photoelectron take-off angles sampled when analyzing AuNPs. The d_H values for the COOH-SAMs on 14nm AuNP are all greater than the corresponding d_H for COOH-SAMs on flat Au for the same reason. The d_H values for C16 COOH-SAMs decrease with increasing AuNP diameter, similar to the trend observed for the XPS C/Au ratios. As mentioned above, this trend is due to surface curvature effects in AuNPs. For C16-COOH SAM on 14nm AuNP, the d_H value was the largest of all samples analyzed due to the combined effect of the wide range of photoelectron take-off angles accepted in the hybrid mode and the NP surface curvature effect.

We varied θ in equation 1 to match d_H and d_E to d_L, thereby determining the corresponding effective take-off angles. The calculated effective take-off angles are shown in Table 4. The AuNPs have a higher effective take-off angle than the flat surfaces. Though a small change, the effective photoelectron take-off angle appears to increase slightly as the size of the AuNP decreases. The overlayer thicknesses and effective photoelectron take-off angles for the C6 COOH-SAMs had the largest errors, likely due to the well-known effect of short chain SAMs not being as well ordered as the longer chain SAMs. The effective photoelectron take-off angle for the C16 COOH-SAM on flat Au measured at 0° in the electrostatic mode was 0°, as expected since the electrostatic mode only collects signals from a narrow range of photoelectron take-off angles for flat surfaces. The fact that all effective photoelectron take-off angles for data collected from flat surfaces in the hybrid mode fall between 35 and 40° indicates that nearly the full range of possible photoelectron take-off angles are accepted by the analyzer in the hybrid mode. This means to accurately measure SAM overlayer thicknesses on flat surfaces the electrostatic mode, with its narrow range of photoelectron take-off angles, must be used. Under these conditions an effective or “magic” photoelectron take-off angle does not need to be used. However, for NP samples where the samples themselves already produce the full range of photoelectron take-off angles, an effective or “magic” photoelectron take-off angle must be used with all analyzer modes to determine an accurate SAM overlayer thickness. Thus, the hybrid mode and its significantly higher count rates can be used for overlayer thickness calculations from NPs. However, the effective photoelectron take-off angle used in those calculations should account for both the range of analyzer acceptance angles as well as the NP curvature effect.

Typical high resolution XPS C1s and S2p spectra from the COOH-SAM/AuNP samples are shown in Figure 3. The carbon and sulfur compositional values and BEs for all the samples are listed in Tables 5 – 8. The hydrocarbon peak from the methylene groups present in the alkane chains was the major carbon species detected, as expected. The C1s peak near ~286eV contained contributions from both the methylene beta to the carboxylic acid (*C-COOH) and the methylene bound to S. The S2p peaks were fit as described in Castner et al. [34], using doublet peaks with a $2p_{1/2}/2p_{3/2}$ ratio of 0.5 and separation of 1.2 eV. Only bound sulfur ($S2p_{3/2}$ BE = 162 eV) was detected in the high resolution S2p spectra of all samples except the C6 COOH-SAM on flat Au and 14nm AuNP. 9.2 % oxidized sulfur (BE = 169.3eV) and 9.9% unbound sulfur (BE = 163.8eV) were detected for C6 COOH-SAM on flat Au and 14nm AuNP samples, respectively. C6 COOH-SAM on flat Au has the smallest XPS C/Au atomic ratio (see Figure 2a) and the highest methylene stretching frequencies (see FTIR-ATR section below) indicating that it is the most disordered of the SAMs. Therefore, sulfur in the C6 COOH SAM is most accessible to ambient oxygen and is expected to be more readily oxidized.

3.3. TOF-SIMS Analysis

The surface chemistries of the COOH-SAMs on the Au surfaces were further characterized with ToF-SIMS. The comparison of the different ToF-SIMS data was investigated by using PCA, a multivariate data analysis technique. [40,41] Figure S3(a), in Supporting Information, shows the first principal component (PC1) scores from analysis of the positive ion spectra from the C16 COOH-SAMs on the AuNP and flat Au surfaces. PC1 accounted for of the 46% variance in the dataset. The 14nm and 25nm AuNP samples had negative PC1 scores, while the 40nm AuNPs and flat Au surface had positive PC1 scores. The PC1 loadings are shown in Figure S3(b), in Supporting Information. The peaks with the highest negative loadings are $C_3H_5^+$, $C_4H_7^+$, $C_3H_7O^+$and $C_3H_7^+$ fragments, which correlate with the C16 COOH-SAMs on the 14nm and 25nm AuNP samples. The fragments with the highest positive loadings are Au containing fragments and short chain hydrocarbon fragments, which correlate with the C16 COOH-SAMs on the 40nm AuNP and flat Au samples.

The PCA results for 14nm AuNP functionalized with C6, C8, C11, and C16 COOH-SAMs are shown in Figure S4(a) and S4(b) (see Supporting Information). PC1 has 46% variance (data not shown) and showed the sample separation based on batch (i.e. day one samples separated from day two samples). All the samples were prepared, handled and analyzed as similar as possible. The causes for the batch-to-batch variations requires further investigation. PC2 showed sample separation based of the different SAM chain length, and it captured 22% of the variance. The 14nm AuNPs with C6 and C8 COOH-SAMs have negative PC1 scores and hence are correlated to fragments with negative loadings. The 14nm AuNPs with a C11 and 16 COOH-SAMs have positive PC1 scores and hence are correlated to fragments with positive loadings. The PCA results from both sets of samples showed that the Au containing ions correlate with the larger AuNPs and flat Au for constant chain length SAMs and with the shorter chain length SAMs on the 14nm AuNPs. On the other hand, the short hydrocarbon fragments generally correlate with smaller AuNPs for constant chain length SAMs and longer chain length SAMs on the 14nm AuNPs.

Using the key fragments identified by PCA, ratios of sum of $C_{1-4}H_xO_y$ ion intensities to Au containing ions were calculated and plotted for all samples. These ratios are shown in Figure 4 for the 14nm AuNPs with different chain length COOH-SAMs and the C16-COOH SAMs on the AuNP and flat Au surfaces. Graham et al. [41] used this method to characterize the assembly, structure and fragmentation patterns of alkanethiol SAMs on flat Au surfaces. The ratio trends as a function of chain length and AuNP diameter in Figure 4 both agree well with the trends observed for the XPS C/Au atomic ratios shown in Figure 2. Explanation for the change in the ToF-SIMS ion ratio with sample type is similar to the explanation

provided for the change in the XPS C/Au atomic ratios with sample type. For example, as the chain length of the carboxylic acid alkanethiol increases the COOH-SAM thickness will increase. This will in turn lead to an increase in the hydrocarbon fragments due to the longer chains and a decrease in the Au containing fragments due to increased attenuation of Au signals by the thicker overlayer. Also, the degree of ordering in the SAM along with the extent of chain-chain interactions can affect the relative yields of the hydrocarbon and Au containing secondary ions. [41] Thus, the variation in ToF-SIMS ion ratio for the C16 COOH-SAMs with AuNP size is likely due to both changes in SAM order as well as surface curvature effects.

3.4. FTIR-ATR Analysis

FTIR-ATR was used to study the crystallinity of the SAMs on the different surface types by monitoring the positions of the CH stretching frequencies. The typical frequencies reported in the literature for a well-ordered, methyl-terminated alkanethiol SAM (CH_3-SAM) on a flat Au surface are below 2920cm^{-1} for CH_2 asymmetric stretching ($\upsilon CH_{2,\ asym}$) and around 2851 cm^{-1} for CH_2 symmetric stretching ($\upsilon CH_{2,\ sym}$). [51,52] These peaks shift to higher values as the van der Waals interaction between the methylene chains decrease. As evidenced by the $\upsilon CH_{2,\ asym}$ at 2916 $cm^{-1}$and the $\upsilon CH_{2,\ sym}$ at 2848 cm^{-1}, the C16 COOH-SAM had a well ordered, crystalline-like structure on the 14nm AuNPs. The FTIR-ATR spectrum for C16 COOH-SAM on 14nm AuNPs is included in the Supporting Information. The UV/VIS measurement (see Supporting Information) and simple color change observation also confirmed that the C16 COOH-SAM on 14nm AuNPs were the most stable in solution. Other prominent peaks in the spectrum represent the OH stretching mode centered at 3244$cm^{-1}$and the carboxylic C=O stretching mode at 1707cm^{-1}. The methylene CH bending peak at 1465cm^{-1} and the methylene rocking peak at 717cm^{-1} were found for the long linear methylene chains in the well-ordered C16 COOH-SAMs. [53] The absence of a peak in the range of 2600–2550cm^{-1} for the S-H stretch mode was consistent with the absence of unbound thiol in the sample.

Figure 5 shows plots of the $\upsilon CH_{2,\ asym}$ for different chain length of COOH-SAMs (C6, C8, C11 and C16) and CH_3-SAMs (C8, C11 and C16) on flat Au surface. Both SAMs had a similar trend where the $\upsilon CH_{2,\ asym}$ decreased with increasing chain length. On flat Au surfaces the CH_3-SAMs had more well-ordered structures (i.e., lower CH_2 asymmetric stretching frequencies) than the corresponding COOH-SAMs of the same chain length. The terminal COOH group is larger than the terminal CH_3 group and can undergo hydrogen bonding with neighboring COOH groups, both of which likely contribute to the decreased ordering observed in the COOH-SAMs compared to the CH_3-SAMs. Also included in the figure is the $\upsilon CH_{2,\ asym}$ value for a C17 CH_3-SAM (2917cm^{-1}) reported by other groups. [51] The $\upsilon CH_{2,\ asym}$ for C16 COOH-SAM on 14nm AuNPs was within experimental error of the literature CH_3-SAM value, indicating the C16 COOH-SAM was well-ordered on the 14nm AuNPs. This value was lower than the values we found for the C16 COOH-SAM on the flat Au surface. This could be related to the COOH head-group having more space to order better on the curved surface than the flat surfaces. For the other COOH-SAMs on the AuNPs either the CH_2 asymmetric stretching peaks were too weak (C6 COOH-SAM) or too variable (C8 COOH and C11 COOH-SAMs) to obtain good measures of the peak position.

4. Conclusions

A set of well-defined functionalized AuNPs have been prepared and characterized by XPS, ToF-SIMS, TEM, FTIR-ATR and UV/Vis. Dialysis purification compared to typical centrifugation/re-dispersal purification was found to produce higher quality COOH-SAMs on the AuNPs (fewer physisorbed thiol molecules, less unbound sulfur and less oxidized sulfur) and COOH-SAM/AuNPs that were more resistant to aggregation. The effects of

systematically varying the COOH-SAM chain length and AuNP diameter were investigated. Holding the AuNP size constant and increasing the SAM chain length resulted in both increased XPS C/Au atomic ratios and increased ToF-SIMS intensity ratios of the ($C_{1–4}H_xO_y$ ions)/(Au-containing ions). Holding the COOH-SAM chain length constant and decreasing the AuNP size resulted in both increased XPS C/Au atomic ratios and increased ToF-SIMS intensity ratios of the ($C_{1–4}H_xO_y$ ions)/(Au-containing ions). Similarly, the calculated effective take-off angle of the C16 COOH-SAM decreased when increasing the size on the AuNP. FTIR-ATR measurements indicated the C16 COOH-SAMs were well-ordered on 14nm AuNPs. These well-defined and characterized sets of COOH-SAMs/AuNPs are excellent samples for further detailed studies of functionalized AuNPs.

Supplementary Material

Refer to Web version on PubMed Central for supplementary material.

Acknowledgments

This research was supported by NIH grants GM-074511 and EB-002027 (NESAC/Bio). SDT thanks NSF for an IGERT fellowship.

References

1. Daniel, M-Ca; Astruc, D. Chem Rev (Washington, DC, U S). 2004; 104:293.
2. Brust M, Kiely CJ. Colloids Surf, A. 2002; 202:175.
3. Duan C, Cui Hua, Zhang Zhifeng, Liu Bo, Guo Jizhao, Wang Wei. J Phys Chem C. 2007; 111:4561.
4. Frens G. Nature (London), Phys Sci. 1973; 241:20.
5. Frydman A, Castner DG, Schmal M, Campbell CT. J Catal. 1995; 157:133.
6. Giersig M, Mulvaney Paul. Langmuir. 1993; 9:3408.
7. Hostetler MJ, Wingate Julia E, Zhong Chuan-Jian, Harris Jay E, Vachet Richard W, Clark Michael R, Londono J David, Green Stephen J, Stokes Jennifer J, Wignall George D, Glish Gary L, Porter Marc D, Evans Neal D, Murray Royce W. Langmuir. 1998; 14:17.
8. Luedtke WD, Landman U. J Phys Chem B. 1998; 102:6566.
9. Ratner, BD.; Castner, DG. Electron Spectroscopy for Chemical Analysis. In: Gilmore, JCVaI, editor. Surface Analysis—The Principal Techniques. 2. John Wiley and Sons; Chichester: 2009. p. 47
10. Sau TK, Pal Anjali, Jana NR, Wang ZL, Pal Tarasankar. J Nanopart Res. 2001; 3:257.
11. Turkevich J, Stevenson Peter C, Hillier James. Discuss Faraday Soc. 1951; (11):55.
12. Zhang Z-F, Cui Hua, Lai Chun-Ze, Liu Li-Juan. Anal Chem. 2005; 77:3324. [PubMed: 15889925]
13. Eustis S, El-Sayed MA. Chem Soc Rev. 2006; 35:209. [PubMed: 16505915]
14. Grainger DW, Castner DG. Adv Mater (Weinheim, Ger). 2008; 20:867.
15. Baer DR, Gaspar DJ, Nachimuthu P, Techane SD, Castner DG. Anal Bioanal Chem. 396:983. [PubMed: 20052578]
16. Luedtke WD, Landman U. J Phys Chem. 1996; 100:13323.
17. Shard AG, Wang J, Spencer SJ. Surf Interface Anal. 2009; 41:541.
18. Baer DR, Engelhard MH. J Electron Spectrosc Relat Phenom. :178–179. 415.
19. Chen S, Kimura K. Langmuir. 1999; 15:1075.
20. Jahn W. Journal of Structural Biology. 1999; 127:106. [PubMed: 10527899]
21. Shi W, Sahoo Y, Swihart MT. Colloids and Surfaces, A: Physicochemical and Engineering Aspects. 2004; 246:109.
22. Aslan, KaVHP-L. Langmuir. 2002; 18:6059.
23. Weisbecker CS, Merritt MV, Whitesides GM. Langmuir. 1996; 12:3763.

24. Mangeney C, Ferrage Fabien, Aujard Isabelle, Marchi-Artzner Valerie, Jullien Ludovic, Ouari Olivier, Rekaie El Djouhar, Laschewsky Andre, Vikholm Inger, Sadowski Janusz W. Journal of the American Chemical Society. 2002; 124:5811. [PubMed: 12010056]
25. Mirkin CA, Letsinger Robert L, Mucic Robert C, Storhoff James J. Nature (London). 1996; 382:607. [PubMed: 8757129]
26. Templeton AC, Wuelfing WP, Murray RW. Accounts of Chemical Research. 2000; 33:27. [PubMed: 10639073]
27. Brust M, Walker Merryl, Bethell Donald, Schiffrin David J, Whyman Robin. Journal of the Chemical Society, Chemical Communications. 1994:801.
28. Kanaras, AG.; Kamounah, Fadhil S.; Schaumburg, Kjeld; Kiely, Christopher J.; Brust, Mathias. Chemical Communications. Cambridge; United Kingdom: 2002. p. 2294
29. Templeton AC, Hostetler Michael J, Warmoth Emily K, Chen Shaowei, Hartshorn Chris M, Krishnamurthy Vijay M, Forbes Malcolm DE, Murray Royce W. Journal of the American Chemical Society. 1998; 120:4845.
30. Isaacs SR, Cutler Erin C, Park Joon-Seo, Lee T Randall, Shon Young-Seok. Langmuir. 2005; 21:5689. [PubMed: 15952810]
31. Cutler EC, Lundin Erik, Garabato B Davis, Choi Daeock, Shon Young-Seok. Materials Research Bulletin. 2007; 42:1178.
32. Lin S-Y, Tsai Yi-Ting, Chen Chien-Chih, Lin Chia-Mei, Chen Chun-hsien. Journal of Physical Chemistry B. 2004; 108:2134.
33. Mendoza SM, Arfaoui Imad, Zanarini Simone, Paolucci Francesco, Rudolf Petra. Langmuir. 2007; 23:582. [PubMed: 17209609]
34. Castner DG, Hinds K, Grainger DW. Langmuir. 1996; 12:5083.
35. Tsao MW, Hoffmann CL, Rabolt JF, Johnson HE, Castner DG, Erdelen C, Ringsdorf H. Langmuir. 1997; 13:4317.
36. Pan S, Castner DG, Ratner BD. Langmuir. 1998; 14:3545.
37. Lee C-Y, Canavan Heather E, Gamble Lara J, Castner David G. Langmuir. 2005; 21:5134. [PubMed: 15896061]
38. Cheng F, Gamble Lara J, Grainger David W, Castner David G. Anal Chem (Washington, DC, U S). 2007; 79:8781.
39. Baio JE, Weidner T, Brison J, Graham DJ, Gamble Lara J, Castner David G. J Electron Spectrosc Relat Phenom. 2009; 172:2.
40. Wagner MS, Castner DG. Langmuir. 2001; 17:4649.
41. Graham DJ, Ratner BD. Langmuir. 2002; 18:5861.
42. Techane SD, Baer DR, Castner DG. In preparation.
43. Werner, WSM.; Smekal, W.; Powell, CJ. NIST Database for the Simulation of Electron Spectra for Surface Analysis, Version 1.0. National Institute of Standards and Technology; Gaithersburg, Maryland: 2010.
44. Smekal W, Werner WSM, Powell CJ. 2005; 37:1059.
45. Powell CJ, Jablonski A, Werner WSM, Smekal W. Applied Surface Science. 2005; 239:470.
46. Gunter PLJ, Gijzeman OLJ, Niemantsverdriet JW. Appl Surf Sci. 1997; 115:342.
47. Kappen P, Reihs K, Seidel C, Voetz M, Fuchs H. Surf Sci. 2000; 465:40.
48. Cumpson PJ, Zalm PC. Surf Interface Anal. 2000; 29:403.
49. Ertl, G.; Kuppers, J. Low Energy Electrons and Surface Chemistry. 2. Weinheim; Deerfield Beack, FL: 1985.
50. Bain CD, Troughton E Barry, Tao Yu Tai, Evall Joseph, Whitesides George M, Nuzzo Ralph G. J Am Chem Soc. 1989; 111:321.
51. Porter MD, Bright Thomas B, Allara David L, Chidsey Christopher ED. J Am Chem Soc. 1987; 109:3559.
52. Walczak MM, Chung Chinkap, Stole Scott M, Widrig Cindra A, Porter Marc D. J Am Chem Soc. 1991; 113:2370.

53. Coates, J. Interpretation of Infrared Spectra, A Practical Approach. In: Meyers, RA., editor. Encyclopedia of Analytical Chemistry. John Wiley & Sons Ltd; Chichester: 2000. p. 10815

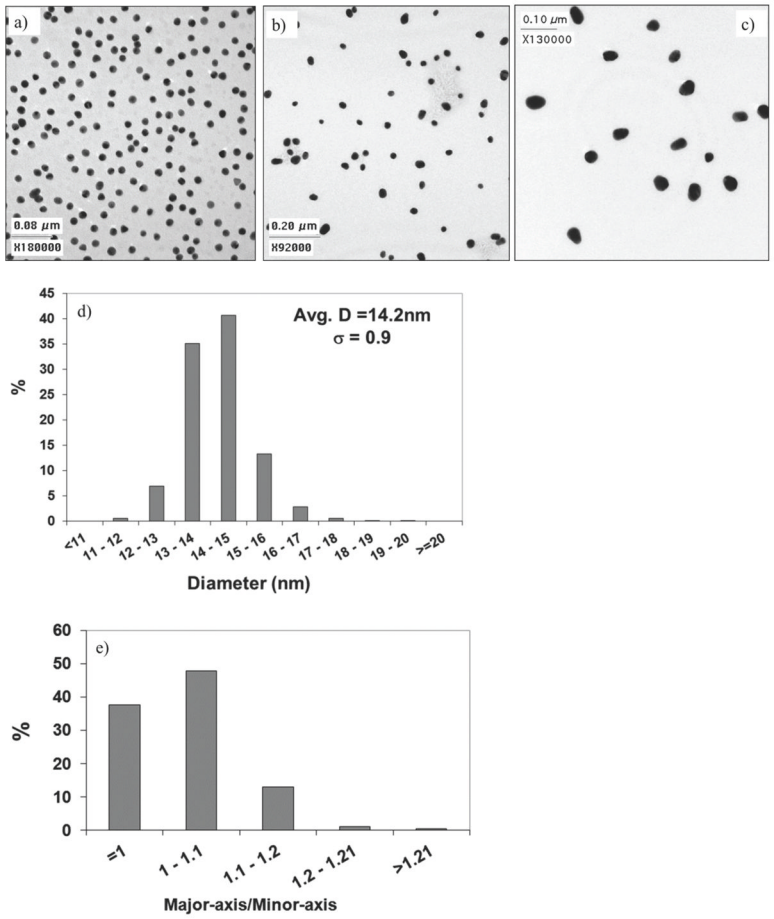

Figure 1.

TEM images for (a) 14nm, (b) 25nm and (c) 40nm citrated stabilized AuNPs, as well ImageJ results for size distribution (d) and circularity (e) for the 14nm AuNPs based on the analysis of 820 AuNPs. The circularity is represented by the ratio of the major axis to the minor axis of the particle.

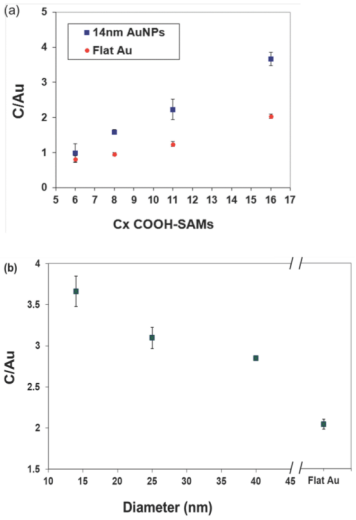

Figure 2.

(a) The XPS C/Au atomic ratio for different chain length COOH-SAMs on 14nm AuNP and flat Au surfaces. (b) The XPS C/Au atomic ratio for C16 COOH-SAMs on AuNP (14, 25 and 40nm) and flat Au surfaces.

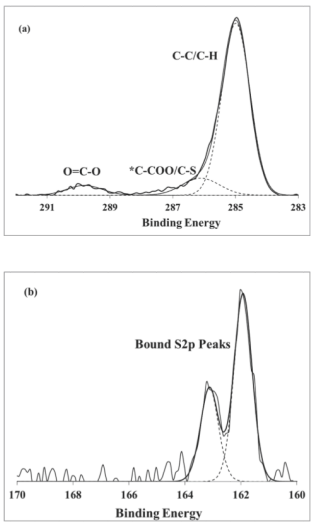

Figure 3.
Typical high-resolution spectra and fits for (a) C1s and (b) S2p peaks from COOH-SAMs on AuNPs and flat Au.

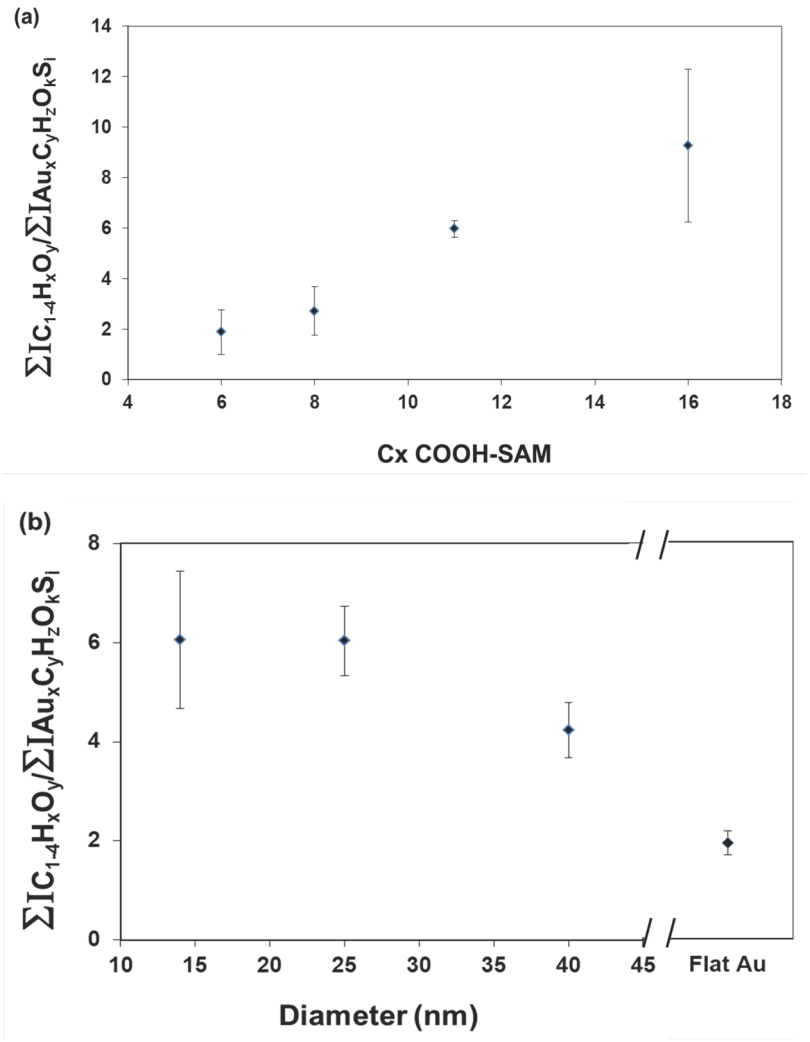

Figure 4.

ToF-SIMS positive ion intensity ratios ($\Sigma C_{1-4}H_xO_y/\Sigma Au_xC_yH_zO_jS_k$) for (a) 14nm AuNPs with C6, C8, C11 and C16 COOH-SAMs and (b) C16 COOH-SAMs on 14, 25 and 40nm AuNP and flat Au surfaces.

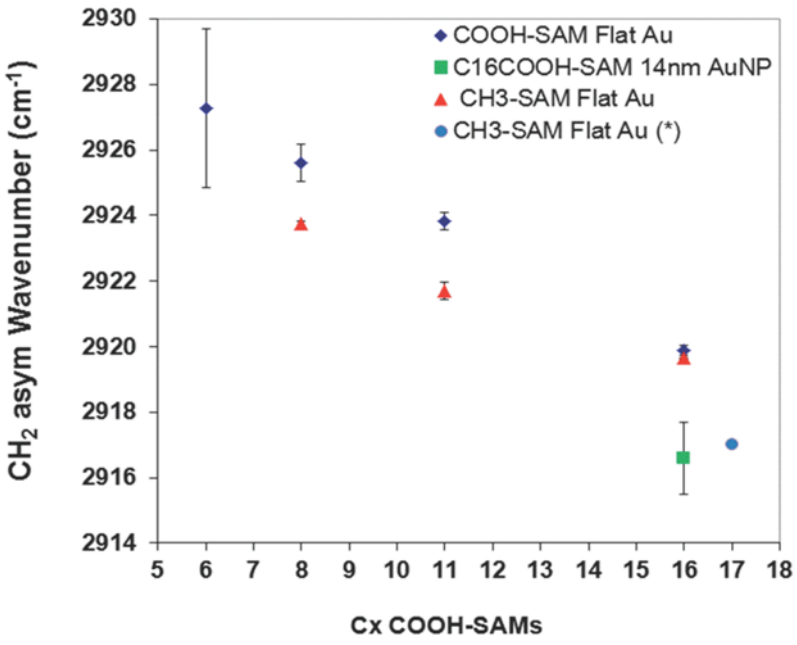

Figure 5.

FTIR-ATR determined CH_2 asymmetric stretching frequencies for C6, C8, C11 and C16 COOH-SAMs and C8, C11 and C16 CH_3-SAMs on flat Au, C16 COOH-SAM on 14nm AuNPs, and (*) C17 CH_3-SAM on flat Au previously reported [51].

Table 1

XPS determined elemental compositions for 14nm AuNP and flat Au surfaces with C6, C8, C11 and C16 COOH-SAMs. Data for AuNP samples were normalized without the Si signal and data for flat surfaces were normalized without the Zn signal, as discussed in the text.

		Atomic % (Std. Dev.)	
		14nm	**Flat Au**
C 1s	C16	70.3 (0.7)	59.5 (0.6)
	C11	60.2 (2.8)	49.0 (0.7)
	C8	53.7 (0.5)	42.3 (0.4)
	C6	43.7 (5.5)	38.1 (2.0)
Au 4f	C16	19.2 (0.9)	29.2 (0.6)
	C11	27.0 (2.7)	39.4 (1.6)
	C8	33.8 (1.4)	44.3 (1.1)
	C6	44.3 (9.7)	46.8 (2.8)
O 1s	C16	9.0 (0.3)	10.0 (0.5)
	C11	10.4 (0.1)	10.2 (1.0)
	C8	9.5 (1.4)	11.7 (0.7)
	C6	8.0 (4.3)	13.0 (1.7)
S 2p	C16	1.5 (0.0)	1.3 (0.0)
	C11	2.3 (0.0)	1.5 (0.1)
	C8	3.0 (0.0)	1.7 (0.2)
	C6	4.0 (0.1)	2.1 (0.3)

Table 2

XPS determined elemental compositions for C16 COOH-SAMs on the AuNP and flat Au surfaces. Data for AuNP samples were normalized without the Si signal and data for flat surface were normalized without the Zn signal, as mentioned in the text.

	Atomic % (Std. Dev.)			
	C 1s	**Au 4f**	**O 1s**	**S 2p**
14nm	70.3 (0.7)	19.2 (0.9)	9.0 (0.3)	1.5 (0.0)
25nm	67.9 (0.7)	21.9 (0.8)	8.5 (0.9)	1.7 (0.2)
40nm	65.7 (0.8)	23.1 (0.1)	9.6 (1.1)	1.6 (0.2)
Flat Au	59.5 (0.6)	29.2 (0.6)	10.0 (0.5)	1.3 (0.0)

Table 3

Apparent overlayer thickness for C_X COOH-SAMs on flat Au and AuNP measured from XPS data acquired in the 'hybrid' and electrostatic modes at a nominal photoelectron take-off angle of 0°. The COOH-SAM thicknesses from the literature are also included in the table.[50]

AuNP Diameter [nm]	COOH-SAM Chain Length	d_H [Å] (Std. Dev.)	d_E [Å] (Std. Dev.)	d_L (Å)
14	6	18 (5)		
	8	24 (1)		
	11	30 (4)		
	16	41 (2)	36	
25	16	37 (1)		
40	16	35 (1)		
Flat Au	6	14 (2)	12 (1)	11
	8	16 (1)	13 (1)	13
	11	20 (1)	17 (3)	16
	16	28 (1)	21 (1)	22

d_H = d based on hybrid mode data

d_E = d based on electrostatic mode data

d_L = d based on literature

Table 4

Effective photoelectron take-off angles for C_X COOH-SAMs on flat Au and AuNP surfaces calculated from XPS data acquired in the 'hybrid' or electrostatic modes.

AuNP Diameter [nm]	COOH-SAM Chain Length	θ_{Et-o} (Std. Dev.) Hybrid Mode		θ_{Et-o} Electrostatic Mode	
		14nm	Flat Au	14nm	Flat Au
14	6	54 (12)	41 (7)		23
	8	58 (1)	38 (2)		0
	11	57 (4)	35 (5)		13
	16	57 (1)	38 (3)	52	0
25	16	53 (1)			
40	16	51 (1)			

θ_{Et-o} = Effective take-off angle needed to match d_H or d_E to d_L.

Table 5

XPS determined carbon species from high-resolution C1s spectra (with standard deviations in parenthesis) for 14nm AuNP and flat Au surfaces with C6, C8, C11 and C16 COOH-SAMs.

		14nm		Flat Au	
		Adj. B.E. (eV)	**Group % (Std. Dev.)**	**Adj. B.E. (eV)**	**Group % (Std. Dev.)**
Hydrocarbon (C–C/C–H)	C16	285.0	82 (2)	285.0	87 (2)
	C11	285.0	78 (3)	285.0	82 (1)
	C8	285.0	77 (3)	285.0	77 (1)
	C6	285.0	72 (3)	285.0	74 (0)
*C–COOH & C–S	C16	286.1	12 (2)	286.1	7 (2)
	C11	286.1	13 (2)	286.1	8 (1)
	C8	286.3	13 (1)	286.1	11 (0)
	C6	286.1	14 (1)	286.1	14 (0)
O=C–O	C16	289.8	6 (0)	289.7	6 (0)
	C11	289.6	9 (2)	289.4	10 (0)
	C8	289.9	9 (2)	289.1	12 (1)
	C6	288.7	14 (2)	289.1	12 (0)

Table 6

XPS determined carbon species from high-resolution C1s spectra (with standard deviations in parenthesis) for C16 COOH-SAMs on the 25 and 40nm AuNPs.

	25nm		40nm	
	Adj. B.E. (eV)	**Group % (Std. Dev.)**	**Adj. B.E. (eV)**	**Group % (Std. Dev.)**
Hydrocarbon (C–C/C–H)	285.0	85 (1)	285.0	85 (0)
*C–COOH & C–S	286.1	10 (1)	286.1	9 (1)
O=C–O	289.9	6 (1)	289.9	6 (1)

Table 7

XPS determined carbon species from high-resolution S2p spectra (with standard deviations in parenthesis) for 14nm AuNP and flat Au surfaces with C6, C8, C11 and C16 COOH-SAMs on 14nm AuNP and flat Au.

		14nm		Flat Au	
		Adj. B.E. (eV)	**Group %**	**Adj. B.E. (eV)**	**Group %**
Bound Sulfur	C16	161.9	100	161.9	100
	C11	162.2	100	162.0	100
	C8	162.1	100	161.9	100
	C6	161.8	90	162.0	91
Unbound Sulfur	C16	nd	nd	nd	nd
	C11	nd	nd	nd	nd
	C8	nd	nd	nd	nd
	C6	163.8	10	nd	nd
Oxidized Sulfur	C16	nd	nd	nd	nd
	C11	nd	nd	nd	nd
	C8	nd	nd	nd	nd
	C6	nd	nd	169.3	9

nd = not detected

Table 8

XPS determined carbon species from high-resolution S2p spectra for C16 COOH-SAMs on the 25 and 40nm AuNPs.

	25nm		40nm	
	Adj. B.E. (eV)	**Group %**	**Adj. B.E. (eV)**	**Group %**
Bound Sulfur	162.0	100	161.9	100
Unbound Sulfur	nd	nd	nd	nd
Oxidized Sulfur	nd	nd	nd	nd

nd = not detected